Lab on a Chip

PAPER

View Article Online
View Journal

Cite this: DOI: 10.1039/d5lc00361j

Evaluating caplacizumab's potential to mitigate thrombosis risk in aortic valve stenosis: a microfluidic and computational approach

Saeedreza Zeibi Shirejini, [ab] Mehrdad Khamooshi,[bc] Damien Riska,[f] Martin Nikolov,[e] Marjan Azimi,[b] Shiyen L. Perera,[abe] Josie Carberry,[b] Karen Alt, [a] Shaun D. Gregory†*[bc] and Christoph E. Hagemeyer †*[ad]

Aortic valve stenosis is a progressive cardiovascular disease associated with increased thrombotic risk due to abnormal blood flow patterns. Current management often culminates in valve replacement surgery, demonstrating the need for less invasive therapeutic options. This study investigates the potential of caplacizumab, a von Willebrand factor (vWF) inhibitor, in mitigating thrombosis risk in a microfluidic model of aortic valve stenosis. We employed a novel microfluidic model simulating the hemodynamics of healthy, moderate, and severe stenotic conditions, complemented by computational fluid dynamics simulations (CFD) and conventional platelet function assays. Microfluidic experiments revealed that shear gradients play a critical role in platelet aggregation, with accumulation intensifying as stenosis severity increased, even under constant peak shear rates. Caplacizumab demonstrated high specificity for vWF-mediated platelet aggregation, significantly inhibiting ristocetin-induced aggregation while not affecting ADP-induced aggregation. At an effective concentration (30 nM), caplacizumab reduced platelet coverage by up to 90% in high shear conditions (4500 s^{-1}) and effectively mitigated shear gradient-dependent platelet aggregation across all stenotic conditions. These findings highlight caplacizumab's therapeutic potential for thrombosis prevention in patients with aortic valve stenosis, offering a foundation for personalized antithrombotic approaches that could potentially reduce thrombotic complications associated with the disease.

Received 14th April 2025,
Accepted 29th July 2025

DOI: 10.1039/d5lc00361j

rsc.li/loc

Introduction

Cardiovascular diseases represent a significant global health challenge, with thrombosis-related complications imposing a substantial burden. Thrombotic disorders, encompassing conditions like thrombotic thrombocytopenic purpura (TTP), coronary artery disease (CAD), arterial thrombosis, and valvular heart disease, are characterised by the uncontrolled formation of blood clots, potentially leading to life-threatening consequences. Among these, aortic stenosis (AS) stands out as the most prevalent valvular heart disease in developed countries.[1] AS is a progressive disease characterised by the calcification and fibrosis of the aortic valve, leading to obstruction of blood flow.[2] The thickening and constriction of the aortic valve causes significant shear stress on blood cells in the vicinity of the valve opening. Under normal physiological conditions, shear rates in the aortic valve typically range from 100–1000 s^{-1}, but stenotic valves can generate pathological shear rates exceeding 3000 s^{-1}.[3] When shear rates surpass 1500–3000 s^{-1}, platelet activation occurs through shear-induced unfolding of von Willebrand factor (vWF), leading to increased risk of thrombosis formation.[4]

In aortic valve stenosis, platelet activation and aggregation, as well as von Willebrand factor (vWF) unfolding, occur due to elevated shear forces in the stenotic region.[5] While high shear forces exist in both acceleration and deceleration zones, the deceleration region is particularly thrombogenic.[6] As blood flows through the stenotic region, it experiences a rapid acceleration followed by a sudden deceleration. High shear stress in the stenotic region induces conformational changes in von Willebrand factor (vWF), exposing the A1 domain for direct binding to platelet GPIbα

[a] Australian Centre for Blood Diseases (ACBD), Monash University, Melbourne, Victoria, Australia. E-mail: christoph.hagemeyer@monash.edu
[b] Cardio-Respiratory Engineering and Technology Laboratory (CREATElab), Mechanical and Aerospace Engineering, Monash University, Clayton, Victoria, Australia
[c] Centre for Biomedical Technologies and School of Mechanical, Medical and Process Engineering, Queensland University of Technology, Brisbane, QLD, Australia. E-mail: shaun.gregory@qut.edu.au
[d] Monash Biomedical Imaging, Monash University, Clayton, Victoria, Australia
[e] Mechanical and Aerospace Engineering, Monash University, Clayton, Victoria, Australia
[f] Chemical and Biomedical Science, Monash University, Clayton, Victoria, Australia
† Christoph E. Hagemeyer and Shaun D. Gregory shared joint corresponding authorship.

receptors. This shear-induced platelet aggregation (SIPA) occurs through shear-dependent vWF–GPIbα interactions that are rapid and independent of classical platelet activation pathways.[7] In aortic valve stenosis, while high shear initiates vWF unfolding and GPIbα binding in the stenotic region, the downstream deceleration zone provides favorable conditions for platelet cluster stabilization due to lower dispersive forces and increased residence time.[8]

The sudden change in shear stress activates mechanosensitive receptors on the platelet surface,[9] while the elongational flow causes significant stretching and unfolding of vWF multimers, exposing their hidden binding sites for platelets.[10] These factors, along with the altered fluid dynamics in the deceleration region, promote platelet aggregation and thrombus formation downstream of the stenosis (Fig. 1).[11] Understanding of the complex mechanisms that underlie thrombosis formation in aortic valve disorders is essential for the development of effective therapeutic and preventive strategies.

Existing interventions for aortic valve stenosis primarily centre around surgical interventions such as valve replacement or repair.[12] While effective, these procedures entail inherent risks and might not be feasible for all patients, especially those with significant comorbidities or contraindications for surgery. Furthermore, pharmacological therapies aimed at mitigating platelet aggregation in this specific context remain relatively limited. The fundamental challenge of preventing shear-induced thrombosis while avoiding systemic bleeding complications in aortic stenosis highlights the clinical need for targeted antithrombotic approaches that can respond to local hemodynamic conditions.[13] In recent years, significant progress has been made in the development of inhibitors targeting the GPIb-IX-V receptor complex and vWF, aiming to curtail thrombus formation. Notably, inhibitors such as caplacizumab (Cablivi), ARC1779, and anfibatide have emerged as promising agents targeting the vWF–GPIbα interaction, effectively reducing thrombus formation.[14–16]

Caplacizumab, a bivalent NANOBODY® molecule against vWF, helps prevent blood clots by blocking the interaction between vWF and the GPIbα receptor. This is especially effective under high-shear conditions, where it limits platelet adhesion to injured vessel walls. It was approved by the European Medicines Agency in 2018 and by the US Food and Drug Administration in 2019 for the treatment of acquired TTP (aTTP). Extensive nonclinical and clinical studies have shown that caplacizumab is highly effective in preventing platelet adhesion and aggregation, significantly reducing thrombotic events while minimising the risk of bleeding complications.[17]

While caplacizumab shows promising potential in addressing thrombosis, understanding its effectiveness within the complex hemodynamic environment of stenotic aortic valves requires sophisticated experimental approaches. Clinical evaluations demonstrate the drug's overall efficacy but provide limited insight into how it functions within the intricate flow environments characteristic of valve stenosis. To bridge this gap between pharmacological action and clinical outcomes, complementary technologies that can replicate and analyze the pathophysiological flow conditions of stenotic valves are essential. Conventional models, such as parallel-plate flow chambers[18] and cone-and-plate shearing devices,[19] often fall short in capturing the intricate flow dynamics and shear stress profiles associated with aortic valve disorders.

To overcome these limitations, microfluidic platforms offer the ability to create controlled environments with precise shear

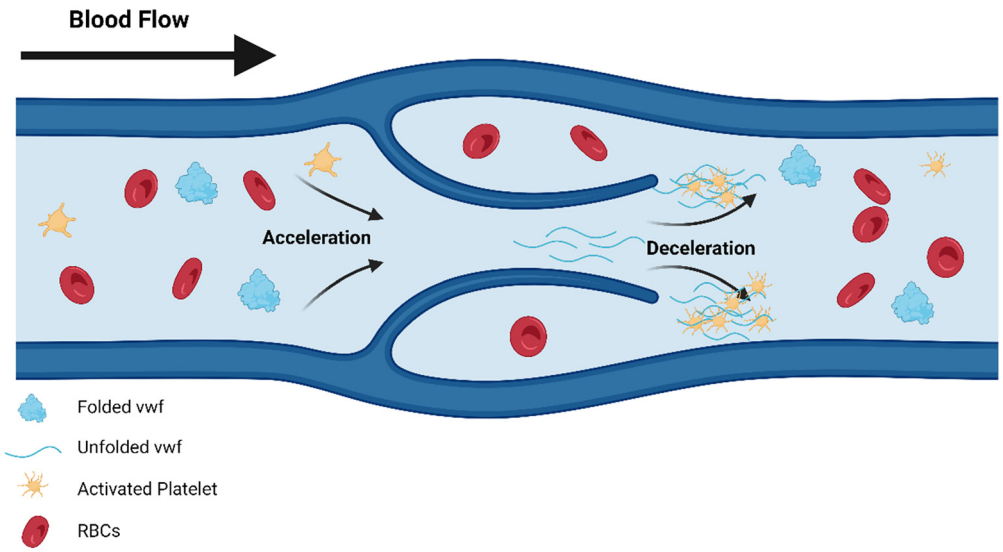

Fig. 1 Shear-induced platelet aggregation in aortic valve stenosis. The stenotic region generates high shear stress, triggering von Willebrand factor (vWF) unfolding and rapid binding to platelet GPIbα receptors without requiring platelet activation. The downstream deceleration zone enables platelet cluster stabilization due to lower dispersive forces and prolonged platelet residence time. Fig. 1 created with **https://BioRender.com**.

stress levels, gradients, and stenotic geometries that mimic the complex flow dynamics found in diseased valves, enabling detailed investigation of platelet aggregation under physiologically relevant conditions. When coupled with computational fluid dynamics (CFD),[20,21] these experimental systems provide comprehensive insights into how local hemodynamic parameters, particularly shear gradients and flow deceleration zones, influence thrombotic processes and therapeutic interventions.

While prior studies have advanced thrombosis modeling using CFD simulations or microfluidic platforms,[22–26] these approaches face critical limitations when applied to aortic stenosis. CFD-only models characterize shear environments but lack biological validation, while traditional *in vitro* systems such as parallel-plate and cone-and-plate devices typically apply uniform shear but fail to replicate the spatially heterogeneous and gradient-driven flow fields characteristic of stenotic valves. Moreover, existing approaches emphasize peak wall shear stress without systematically examining shear gradients or incorporating specific geometries with therapeutic validation. These limitations restrict mechanistic understanding of gradient-driven thrombus formation and hinder evaluation of targeted therapeutics such as caplacizumab under stenosis-relevant hemodynamic conditions.

This study provides novel insights into thrombosis dynamics in aortic valve stenosis through a uniquely integrated experimental–computational framework. By combining stenosis geometries with CFD modeling and real-time platelet aggregation imaging under defined shear gradients, we evaluate caplacizumab's efficacy in mitigating shear-induced thrombosis. This platform not only expands on previous peak shear-focused models but also bridges a key translational gap by capturing the interplay between hemodynamic forces and therapeutic action in stenotic cardiovascular disease.

Materials and methods

Materials

Caplacizumab was provided by Sanofi (Cablivi, 10 mg mL^{-1}). Ristocetin (Helena Biosciences, Australia) and ADP (final concentration of 10 μM; Sigma-Aldrich) were used as platelet agonists. Eptifibatide (Integrilin, 75 mg/100 mL as acetate; Merck Sharp and Dohme, Australia) served as a therapeutic comparator representing standard GPIIb/IIIa inhibition, used at a final concentration of 5 μM. Collagen type I/III blend (ratio 1 : 1, 100 μg mL^{-1} final concentration) was obtained from Sigma-Aldrich. $DiOC_6$ (3,3′-dihexyloxacarbocyanine iodide, 0.5 μg mL^{-1} final concentration) was purchased from Sigma-Aldrich. APC-conjugated fluorescent microspheres beads (6 μm diameter, BD Biosciences) were used as negative controls to validate biological specificity of platelet aggregation. Beads were used at a final concentration of 2×10^6 beads per mL. For microfluidic device fabrication, SYLGARD™ 184 Silicone Elastomer kit (Dow SYLGARD) was used. Antibodies used were Alexa Fluor 546-conjugated anti-VWF (#A0082, rabbit polyclonal antibody anti-human vWF, Dako) and APC-conjugated anti-CD42b (Clone HIP1, IgG1, kappa, eBioscience). Tri-sodium citrate dihydrate (Merck), paraformaldehyde (reagent grade, Sigma-Aldrich), and bovine serum albumin (≥96% purity, Sigma-Aldrich) were used. All other chemicals and reagents were of analytical grade.

Equipment used included an AggRam platelet aggregometer (Helena Laboratories, USA), Aurora Northern Lights flow cytometer (Cytek Biosciences, Fremont, CA), Nikon Ti-E inverted fluorescence microscope equipped with a 20× objective (NA 0.75) and sCMOS Andor Zyla 4.2 PLUS camera (Oxford Instruments), and a Legato 130 programmable syringe pump (KD Scientific, USA). Data analysis was performed using FlowJo software and GraphPad Prism v9.1 (GraphPad Software, San Diego, CA).

Reagents and blood sample preparation

Blood was collected from healthy volunteers with no history of cardiovascular disease and no medication use within 14 days, after obtaining full written informed consent, in compliance with the Monash University Ethics guidelines. This study was approved by the Medical Research Ethics Committee of Monash University, Australia (Project ID: 35867). Informed consent was obtained from all volunteers prior to donation of blood. Blood was collected *via* venipuncture into syringes pre-loaded with 3.2% sodium citrate (9 : 1, v/v). For platelet-rich plasma (PRP) preparation, whole blood was centrifuged at 180 × *g* for 10 minutes at room temperature. Platelet-poor plasma (PPP) was obtained by further centrifugation of the remaining PRP at 3000 × *g* for 15 minutes.

Microfluidic device design and fabrication

The microfluidic device was designed to replicate key features of the human aortic valve, based on Swanson and Clark's dimensional parameters.[27] We developed three stenosis geometries representing healthy (30% occlusion), moderate (55% occlusion), and severe (80% occlusion) conditions. The main channel width was 240 μm, length 20 mm, and height 58 μm, with stenotic region openings of 0.168 mm, 0.108 mm, and 0.048 mm for healthy, moderate, and severe conditions, respectively.

The PDMS microfluidic device was fabricated using standard photolithography at the Melbourne Centre for Nanofabrication (MCN). The microchannel layout, designed in AutoCAD, was transferred onto a photomask and patterned onto a silicon wafer coated with SU-8 photoresist to achieve a channel depth of 58 μm. After soft-baking to evaporate solvents, the photoresist was selectively crosslinked by UV exposure through the photomask, followed by a post-exposure bake. Unexposed photoresist was removed in a developer, leaving a patterned silicon master. The master was silanised to facilitate PDMS release. A 10 : 1 mixture of PDMS prepolymer and curing agent was poured over the master and cured at 80 °C for 4 hours (Fig. 2). Once cured, the PDMS layer was peeled off, inlet and outlet ports were punched, and the device was sealed with a glass coverslip.[28]

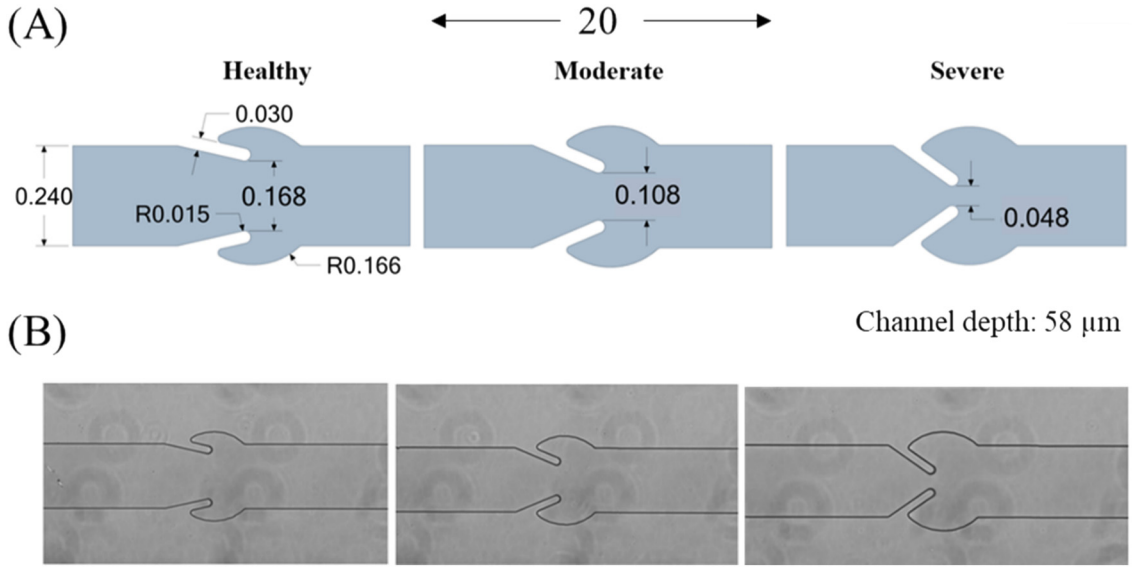

Fig. 2 Microfluidic device geometries and fabricated channels. (A) Schematic representation of the three stenosis geometries: healthy (30% occlusion, opening 0.168 mm), moderate (55% occlusion, opening 0.108 mm), and severe (80% occlusion, opening 0.048 mm). All channels have a total length of 20 mm, width of 0.240 mm, and a constant height of 58 μm, with radius of curvature specified for stenosis transitions. (B) Brightfield microscopy images of the fabricated microfluidic channels showing the three stenosis geometries: healthy (left), moderate (middle), and severe (right).

Computational fluid dynamics (CFD) simulations

Steady flow conditions were employed to capture peak shear rates where shear-induced platelet aggregation is most pronounced in stenotic regions. This approach enables precise control of shear parameters and direct comparison with experimental validation studies. Casa and Ku experimentally validated that steady flow at matched shear rates effectively models pulsatile arterial thrombosis, showing no significant differences in key thrombotic parameters between pulsatile and steady conditions.[29]

CFD simulations were employed to complement experimental microfluidic analyses, providing detailed insights into fluid dynamics within the aortic valve stenosis microchannels. The simulations numerically solved the continuity and Navier–Stokes equations for laminar flow to predict velocity fields, shear rate, and shear stress profiles across the computational domain. The microchannel geometry was discretised using a poly-hexcore meshing scheme in Fluent Meshing 2023R2, resulting in a high-resolution finite volume mesh with 8 103 340 cells, allowing for precise capture of complicated flow details. A mesh convergence study confirmed the adequacy of the mesh resolution, with the root mean squared error in velocity magnitude and wall shear stress remaining below 1%. Simulations were conducted in ANSYS Fluent using the semi-implicit method for pressure-linked equations (SIMPLE) algorithm to solve the coupled system of equations.

Blood was modelled as an incompressible, Newtonian fluid with a density of 1050 kg m^{-3} and a dynamic viscosity of 0.00345 Pa s. This assumption is valid for shear rates exceeding 500 s^{-1}, where blood viscosity plateaus and demonstrates near-Newtonian behavior.[23,30] All simulated flow conditions in this study (562–4500 s^{-1}) fall within this validated regime. Previous studies have reported that shear rates in stenotic valves can reach over 3000 s^{-1} in severe cases,[31,32] substantially exceeding the normal physiological range of 100–1000 s^{-1} in healthy valves.[33] For our computational analysis, flow rates of 0.83, 1.66, 3.33, 6.66, and 13.3 μL min^{-1} were simulated across all stenosis models to characterize how geometrical differences affect shear rate distributions and gradients at constant input flow. These flow rates were selected to generate shear rate ranges comparable to those observed *in vivo*, allowing our model to capture the key hemodynamic features relevant to platelet aggregation despite the geometric simplification. Boundary conditions included a no-slip condition at channel walls and a specified pressure boundary (0 Pa) at the outlet.

The CFD model was used to establish flow rate-shear rate relationships for experimental design and does not simulate cellular-level interactions or thrombosis formation. We acknowledge that for channel dimensions below ~100 μm, including the 48 μm severe stenosis model, discrete cellular phenomena become dominant and are not captured by continuum models.[34,35]

Platelet aggregation assay

Platelet aggregation assays were performed using both ristocetin and ADP as agonists. Ristocetin was chosen for its ability to mimic the effect of high shear stress on vWF unfolding, exposing the A1 domain for platelet binding.[36,37] ADP-induced aggregation was used as a control to demonstrate the specificity of caplacizumab's effect on vWF-mediated platelet aggregation. PRP and PPP were prepared as previously described. The

platelet count in PRP was adjusted to 250×10^9 L^{-1} using PPP to ensure consistent platelet concentrations across experiments.

Light-transmission platelet aggregometry was conducted using AggRam systems (Helena Laboratories, USA) at 37 °C with constant stirring at 600 rpm. For calibration, 300 μL of blank PPP was placed in a cuvette under stirring conditions. To assess platelet aggregation, ristocetin (1.5 mg mL^{-1} final concentration; Helena Biosciences, Australia) and ADP (10 μM final concentration; Sigma-Aldrich) were added to the PRP solution in separate channels. The final volume was adjusted to 300 μL with PBS, and all runs were performed in duplicates. Before agonist addition, caplacizumab was introduced to pre-warmed (37 °C) PRP at concentrations ranging from 0 to 50 nM and incubated for 20 minutes. Platelet aggregation responses were assessed with and without caplacizumab. The amplitude of aggregation was determined 10 minutes after agonist addition as an indicator of the degree of platelet aggregation. Light transmission data were expressed as mean ± SEM percentage of platelet aggregation and plotted using HemoRam 1.3 software.

Flow cytometry analysis of platelet-vWF binding

The effect of caplacizumab on ristocetin-induced platelet activation and vWF binding was investigated using flow cytometry. Diluted PRP (50 μL, 1 : 20 dilution) was added to a 50 μL reaction mix containing caplacizumab (15 nM) in PBS. After 10-minute incubation at room temperature, ristocetin (1.5 mg mL^{-1}) was added, followed by Alexa Fluor-conjugated anti-vWF antibody (1 μL) and APC-conjugated anti-CD42b (2 μL; GPIb receptor marker). The samples were incubated for 20 minutes at room temperature, and reactions were stopped with 200 μL of 1% PFA fixation solution. Data acquisition was performed with Aurora, Northern Lights (Cytek Biosciences, Fremont, CA) and analysed with FlowJo software. VWF binding to platelets was detected by the median fluorescent intensity (MFI).

Microfluidic analysis of high shear-induced platelet aggregation

Prior to experiments, channels were functionalised with collagen types I and III solution (1 : 1 v/v, 100 μg mL^{-1}) for 1 hour at room temperature, followed by blocking with 2% bovine serum albumin (w/v) for 30 minutes to prevent non-specific binding. Channels were thoroughly rinsed with PBS between steps. Citrate-anticoagulated human whole blood was collected and used within 4 hours. Blood samples were incubated with $DiOC_6$ (0.5 μg mL^{-1}) for platelet visualization and caplacizumab (or PBS for controls) in the dark for 15 minutes at room temperature. The treated blood was pulled through the collagen-coated microchannels using a programmable syringe pump (Legato 130, KD Scientific, USA) to achieve various ranges of shear rate (562, 1125, 1687, 2250, 3375, and 4500 s^{-1}). For experimental microfluidic studies, flow rates were individually adjusted for each stenosis geometry to achieve targeted shear rates (562–4500 s^{-1}) across all models. Platelet adhesion and aggregation were monitored using a Nikon Ti-E inverted fluorescence microscope (Nikon Inc., Japan) equipped with a sCMOS Andor Zyla camera. Images were captured through a 20× objective lens in the FITC channel at 1-second intervals over 10 minutes.

Platelet coverage area was quantified using FIJI image analysis software, and results were expressed as mean ± SEM percentage of the total surface area. Quantitative image analysis was restricted to regions characterized by elevated shear stress and steep spatial shear gradients, specifically, the stenotic throat and downstream deceleration zone, where vWF unfolding and GPIbα-mediated platelet aggregation are the primary mechanisms of interest for this study. Recessed regions, designed to replicate the anatomical sinuses of Valsalva, were excluded from analysis due to their low-shear and altered flow dynamics, which promote different platelet aggregation dynamics than the high-shear, vWF-mediated mechanisms that are the focus of this investigation.

Statistical analysis

Statistical analysis was conducted using GraphPad Prism V9.1 for Windows (GraphPad Software, Inc., San Diego CA). Unless otherwise specified, all experiments were carried out in triplicate using blood samples from three independent healthy donors, and the data is presented as the mean with standard error of the mean (SEM). To compare two conditions, a *t*-test was employed, while differences among more than two conditions were calculated using a one-way ANOVA, followed by Tukey's multiple comparison test. A *P*-value less than 0.05 was considered indicative of statistical significance.

Results

Platelet aggregation assay

Control samples (without caplacizumab) showed high platelet aggregation in response to both ristocetin (1.5 mg mL^{-1}) and ADP (10 μM), with maximum aggregation of 88.3 ± 4.7% and 83.3 ± 3.9%, respectively. The inhibitory effects of caplacizumab on platelet aggregation were investigated using light transmission aggregometry over a concentration range of 0–50 nM. Caplacizumab demonstrated potent, dose-dependent inhibition of ristocetin-induced platelet aggregation (RIPA). Multiple *t*-tests revealed significant reductions in RIPA compared to control (0 nM) at 10 nM (30.6 ± 14.1%, $p < 0.02$), 15 nM (13.7 ± 1.9%, $p < 0.001$), 20 nM (14.5 ± 1.3%, $p < 0.0001$), 25 nM (14.9 ± 1.8%, $p < 0.002$), 30 nM (14.1 ± 1.2%, $p < 0.002$), and 50 nM (13.5 ± 1.2%, $p < 0.002$). Maximal inhibition was achieved at 15 nM and maintained through higher concentrations (Fig. 3).

In contrast, ADP-induced platelet aggregation remained stable across all caplacizumab concentrations, ranging from 88.3 ± 3.9% at baseline to 83.6 ± 3.6% at 50 nM ($p > 0.05$). Statistical analysis revealed no significant differences in ADP-induced aggregation at any caplacizumab concentration tested (multiple *t*-tests, $p > 0.05$). This selective inhibition pattern highlights caplacizumab's specificity for the VWF-mediated

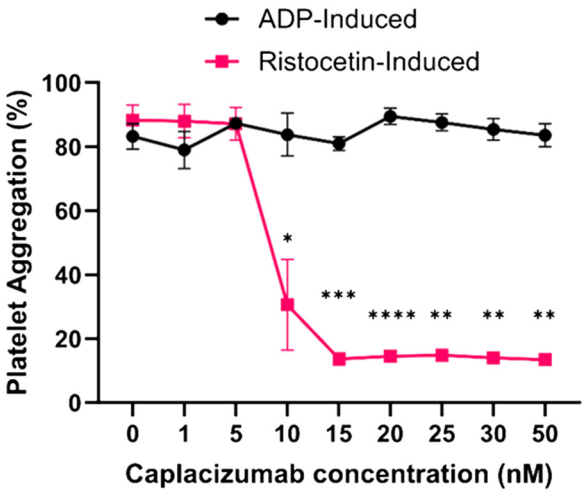

Fig. 3 Dose–response curves of platelet aggregation to caplacizumab. Ristocetin-induced platelet aggregation (red squares) shows concentration-dependent inhibition, while ADP-induced aggregation (black circles) remains unaffected. Data presented as mean ± SEM (n = 3). *$p < 0.05$, **$p < 0.01$, ***$p < 0.001$, ****$p < 0.0001$ *vs.* control (multiple t-tests).

pathway, while preserving normal platelet responses to other physiological agonists.

Flow cytometric analysis of vWF–platelet interaction

Flow cytometry was utilised to investigate caplacizumab's mechanism of action through analysis of vWF binding and GPIb (CD42b) receptor availability. Representative flow cytometry histograms demonstrate the changes in fluorescence intensity for both anti-vWF and anti-CD42b antibodies under different treatment conditions (Fig. 4A). Median fluorescence intensity (MFI) values were normalised to control samples and expressed as fold change. Quantitative analysis revealed that ristocetin treatment (1.5 mg mL^{-1}) significantly increased vWF binding to platelets compared to control (165.4 ± 8.2-fold, $p < 0.0001$). The addition of caplacizumab (15 nM) significantly reduced this ristocetin-induced vWF binding (135.2 ± 15.3-fold, $p < 0.05$ *vs.* ristocetin alone) (Fig. 4B). Higher caplacizumab concentrations (30–50 nM) showed similar inhibitory effects, with no significant additional benefit beyond 15 nM, indicating that maximal inhibition was achieved under these experimental conditions.

Analysis of GPIb receptor availability using anti-CD42b antibody showed no significant changes in receptor expression across all conditions. Neither ristocetin treatment (0.75 ± 0.12-fold *vs.* control, $p > 0.05$) nor the addition of caplacizumab (0.92 ± 0.05-fold *vs.* control, $p > 0.05$) significantly altered CD42b levels, indicating that the vWF–platelet interactions under these conditions do not affect GPIb receptor accessibility.

Evaluation of caplacizumab concentration effects in microfluidic stenosis model

Following the characterization of caplacizumab's effects on vWF–platelet interactions in static conditions, its efficacy was evaluated under physiologically relevant flow conditions using the microfluidic model. Under severe stenosis conditions (with a peak shear rate of 4500 s^{-1} at the stenotic region), three concentrations of caplacizumab (15, 30, and 45 nM) were tested based on the aggregometry and flow cytometry findings. At 15 nM, platelet coverage was reduced to 53.3 ± 10.9% compared to control (68.3 ± 7.3%), though this reduction was not statistically significant (p = 0.3168). However, significant reductions in platelet coverage were achieved at both 30 nM (7.7 ± 1.2% *vs.* control 71.7 ± 6%, $p < 0.01$) and 45 nM (6.2 ± 0.4% *vs.* control 71.1 ± 3%, $p < 0.01$) (Fig. 5). Given that 30 nM provided robust inhibition with no significant additional benefit at 45 nM, this concentration was selected for subsequent microfluidic experiments.

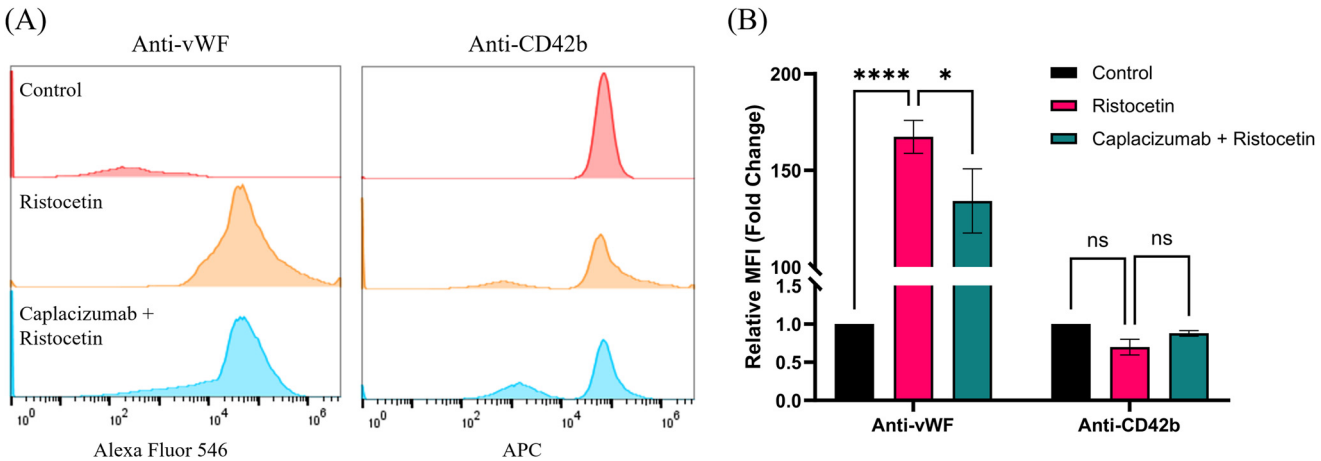

Fig. 4 Flow cytometric analysis of caplacizumab's effect on vWF–platelet interactions. (A) Representative flow cytometry histograms showing anti-vWF (left) and anti-CD42b (right) binding under control (red), ristocetin (orange), and caplacizumab (15 nM) + ristocetin (blue) conditions. (B) Quantification of median fluorescence intensity (MFI) expressed as fold change relative to control. Data presented as mean ± SEM (n = 3). *$p < 0.05$, ****$p < 0.0001$; ns, not significant (one-way ANOVA with Tukey's *post hoc* test).

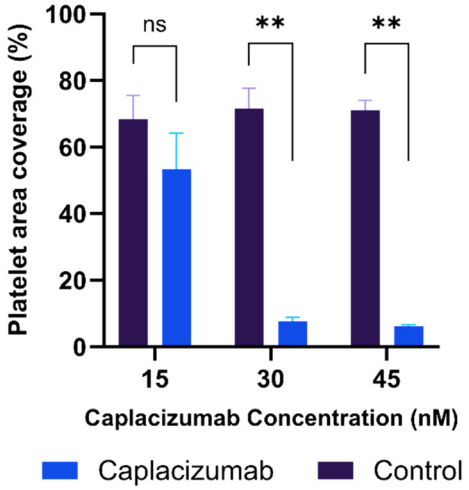

Fig. 5 Dose-dependent inhibition of platelet adhesion by caplacizumab under high shear conditions. Platelet coverage was assessed in severe stenosis geometry at 4500 s^{-1} shear rate. Data presented as mean ± SEM (n = 3). **p < 0.01; ns, not significant (paired t-tests comparing each concentration to its respective control).

The effective caplacizumab concentration used in this study falls within a clinically relevant range. Clinical dosing of caplacizumab (10 mg IV bolus followed by 10 mg SC daily) are well established for acquired thrombotic thrombocytopenic purpura.[38] The selected concentration accounts for the absence of systemic clearance and plasma protein binding *in vitro*, while ensuring robust inhibition of vWF–platelet interactions under high shear conditions (>2250 s^{-1}) that are characteristic of aortic valve stenosis. This concentration supports the translational potential of current findings for potential clinical applications in aortic stenosis.

Computational fluid dynamics analysis of stenotic flow conditions

Computational fluid dynamics (CFD) was employed to characterise the hemodynamic environment across three stenosis geometries (30%, 55%, and 80% occlusion). The CFD simulations revealed distinct patterns in shear rate, wall shear stress, and velocity magnitude that provided mechanistic insights into the observed platelet aggregation behaviour. The velocity field analysis demonstrated progressive velocity gradient with increasing stenosis severity (Fig. 6, bottom row). In the healthy model (30% occlusion), relatively uniform velocity distributions were observed, with peak velocities of approximately 0.04 m s^{-1} (at 13.3 μL min^{-1} inlet flow rate). The flow pattern became increasingly heterogeneous in moderate (55% occlusion) and severe (80% occlusion) stenosis, with peak velocities reaching 0.06 m s^{-1} and 0.15 m s^{-1}, respectively. Notably, the severe stenosis model exhibited highly localised high-velocity regions at the stenotic site, contrasting with the more uniform flow distribution observed in the healthy model.

The shear rate analysis revealed distinct patterns across stenosis severities (Fig. 6, top row). While all models showed elevated shear rates at the stenotic region, the pattern evolved from a moderate elevation in the healthy model to an intense, highly localised peak in the severe stenosis model. Peak shear rates were observed at the stenotic region, with values increasing dramatically with stenosis severity. The relationship between peak shear rate and flow rate, maintained linearity across all stenosis conditions (Fig. 7A), with the severe stenosis model demonstrating a significantly steeper slope (approximately 1616 s^{-1} min μL^{-1}) compared to moderate (528 s^{-1} min μL^{-1}) and mild stenosis geometries (327 s^{-1} min μL^{-1}). At the highest tested flow rate (13.3 μL min^{-1}), peak shear rates reached approximately 22 259 s^{-1} in the severe stenosis model, compared to 7278 s^{-1} and 4500 s^{-1} in the moderate and healthy stenosis models, respectively. Fig. 7B presents the flow rates required to achieve equivalent peak shear rates across all three stenosis models for the experimental studies.

Detailed examination of the shear rate profiles revealed a characteristic biphasic pattern with distinct acceleration and deceleration zones (Fig. 8). In the severe stenosis model, the shear rate gradients exhibited marked asymmetry around the stenotic region ($x \approx 400$ μm). At the highest flow rate (13.3 μL min^{-1}), the acceleration phase generated positive gradients of 2×10^8 s^{-1} μm^{-1}, followed by negative gradients of similar magnitude in the deceleration phase. This gradient pattern was flow rate-dependent, with proportionally lower magnitudes observed at reduced flow rates (*e.g.*, 5×10^7 s^{-1} μm^{-1} at 3.33 μL min^{-1}). The moderate and healthy stenosis models demonstrated qualitatively similar patterns but with substantially reduced gradient magnitude.

Wall shear stress (WSS) analysis revealed characteristic patterns that evolved with increasing stenosis severity (Fig. 6, middle row). Maximum WSS values were consistently observed at the point of maximal constriction in all models, with the severe stenosis model generating the highest local WSS. The WSS distribution showed spatial heterogeneity, particularly in the severe stenosis model, where sharp transitions were observed at the entrance and exit of the stenotic region. The highest shear rate gradients developed at these transition zones, immediately upstream and downstream of the stenosis, and these high-gradient regions corresponded to areas of platelet accumulation observed in our experimental studies, as illustrated in Fig. 9 and 10A, where platelet coverage is highest in the downstream deceleration region.

Shear-induced platelet aggregation and caplacizumab's inhibitory effects

The shear rate-dependent efficacy of caplacizumab reflects the mechanistic transition in platelet aggregation pathways. At lower shear rates (<1000 s^{-1}), platelet aggregation occurs primarily through fibrinogen–αIIbβ3 interactions pathway, with minimal contribution from vWF–GPIbα interactions. However, as shear rates exceed this threshold, mechanical forces unfold vWF, exposing the A1 domain and making GPIbα–vWF binding the dominant aggregation mechanism.[4,39] Under these high-

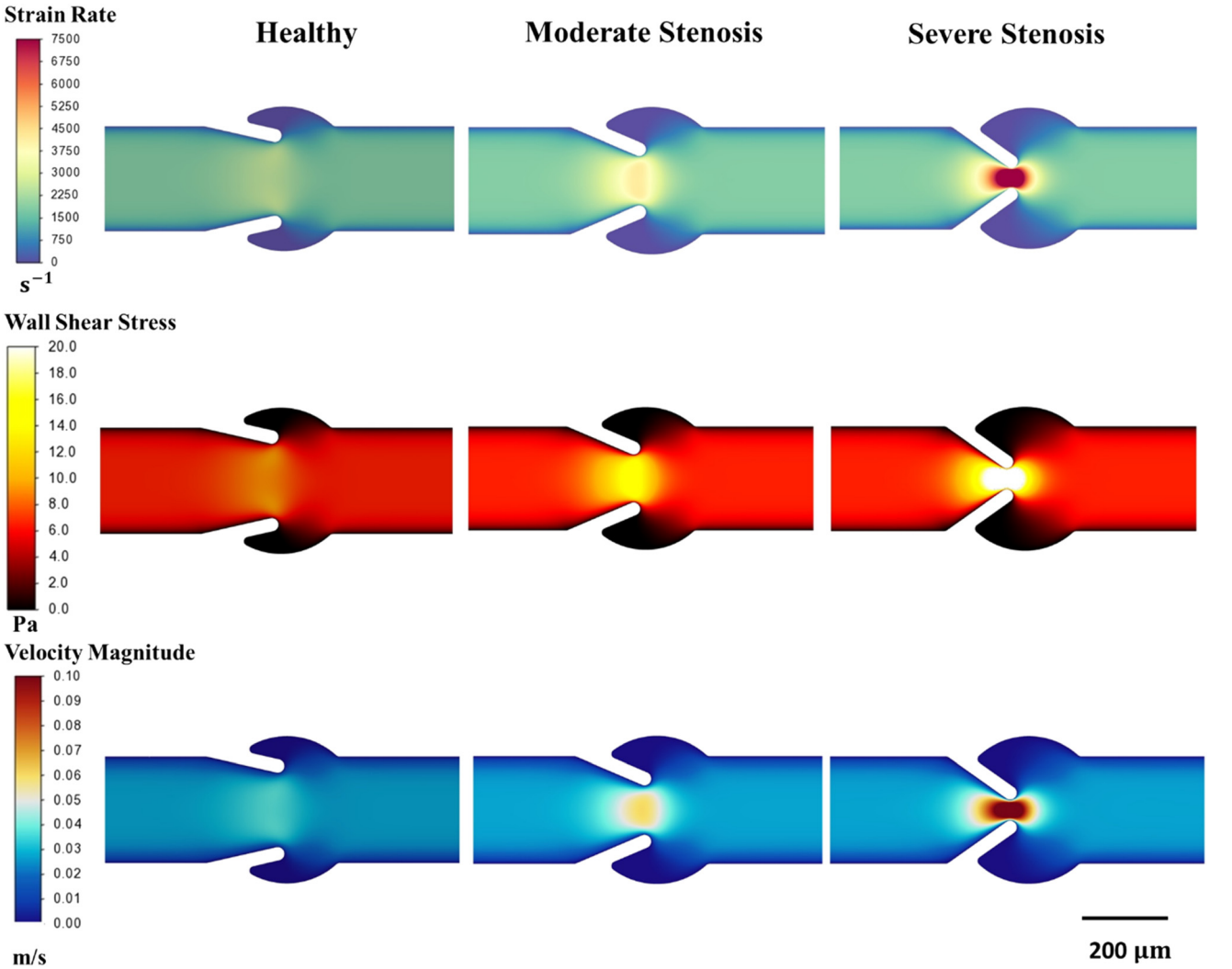

Fig. 6 Spatial distribution of hemodynamic parameters in microfluidic stenosis models, shown for a representative inlet flow rate of 13.3 µL min^{-1}. Contour plots showing shear (strain) rate (top), wall shear stress (middle), and velocity magnitude (bottom) for healthy (30% occlusion), moderate stenosis (55% occlusion), and severe stenosis (80% occlusion) geometries. Colour scales represent magnitude ranges for each parameter.

(A)

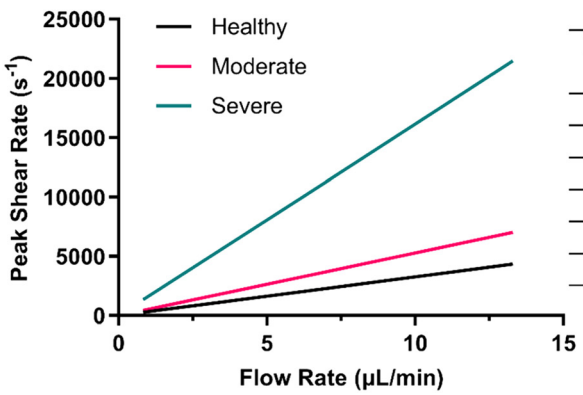

(B)

Peak Shear Rate (s^{-1})	Healthy Flow Rate (µL/min)	Moderate Stenosis Flow Rate (µL/min)	Severe Stenosis Flow Rate (µL/min)
562	1.66	1.03	0.33
1125	3.33	2.05	0.66
1687	4.98	3.08	1
2250	6.66	4.11	1.32
3375	9.99	6.18	2.02
4500	13.3	8.21	2.64

Fig. 7 Flow rate and shear rate relationships across stenosis models. (A) Linear relationship between input flow rate and resulting peak shear rate for each stenosis geometry. (B) Flow rates required to achieve equivalent target peak shear rates across the three stenosis models for experimental platelet studies.

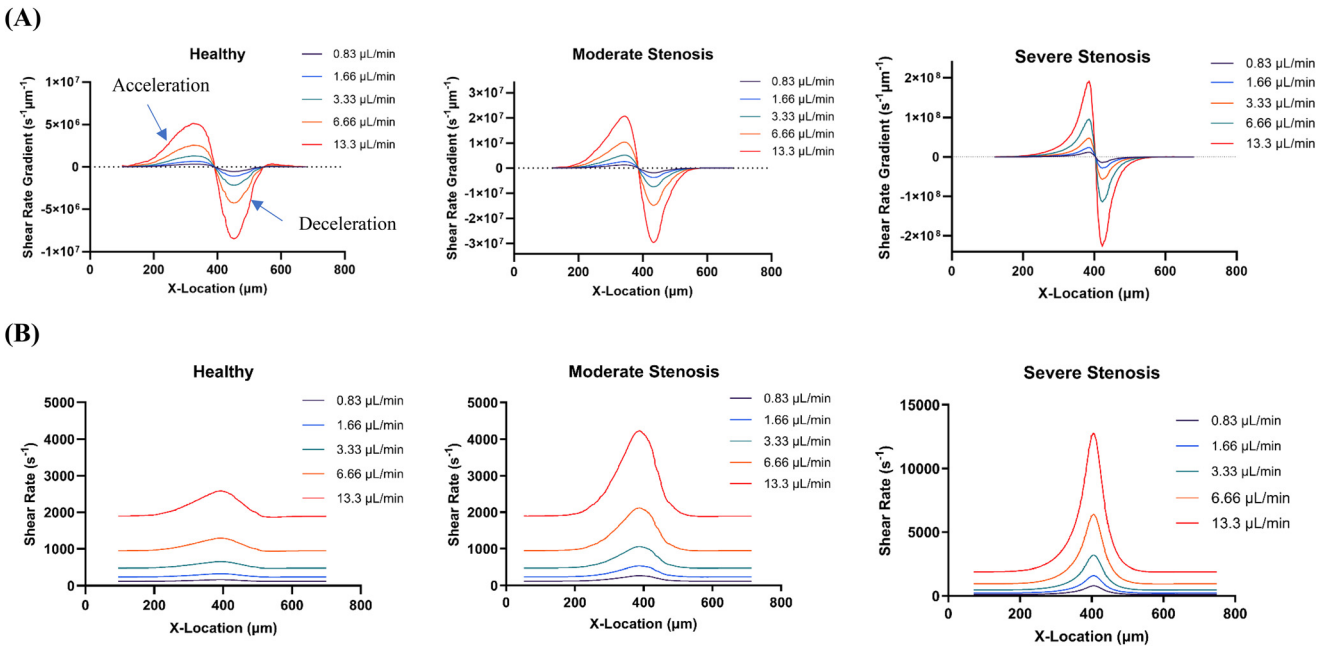

Fig. 8 Shear rate characteristics along the stenosis channel. (A) Shear rate gradients and (B) corresponding shear rate magnitudes for three stenosis geometries at flow rates ranging from 0.83 to 13.3 μL min^{-1}. The *x*-axis indicates the spatial position along the channel length.

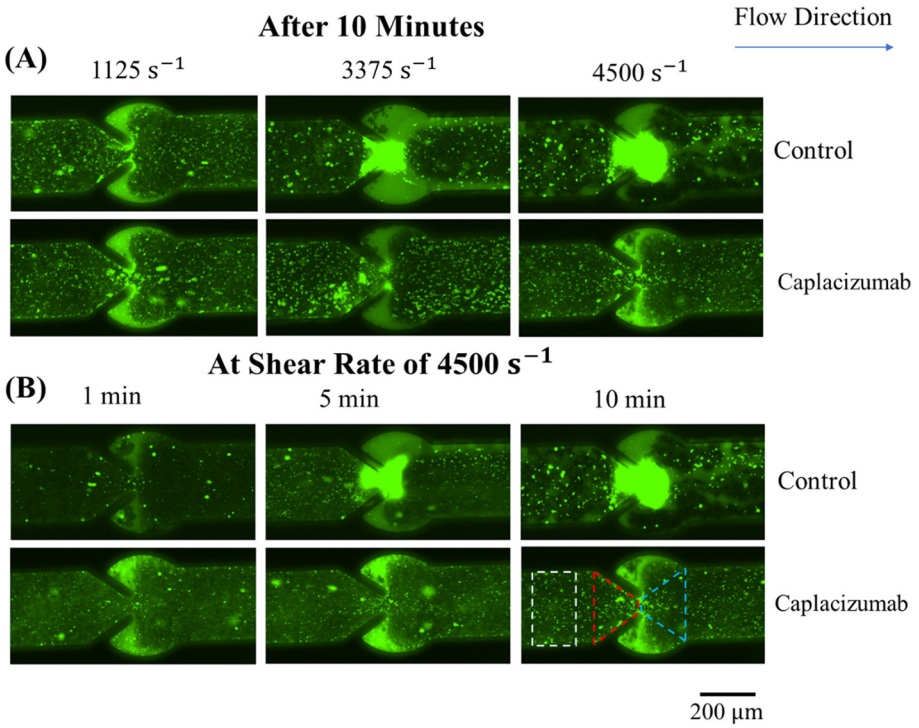

Fig. 9 Effect of caplacizumab on shear-induced platelet aggregation in severe stenosis. (A) Representative fluorescence images after 10 minutes of flow at indicated shear rates for control and caplacizumab-treated samples. (B) Time-course of platelet accumulation at 4500 s^{-1}. The bottom-right image illustrates the regions of interest used for platelet coverage quantification: white dashed rectangle (upstream region), red quadrilateral (acceleration region), and blue quadrilateral (downstream deceleration). $DiOC_6$-labeled platelets appear in green.

shear conditions, caplacizumab effectively blocks this pathway, resulting in significant platelet inhibition while untreated samples show continued aggregation increase.

Based on the CFD characterization of flow fields, which identified critical shear rate thresholds and distributions across different stenosis geometries, microfluidic experiments were

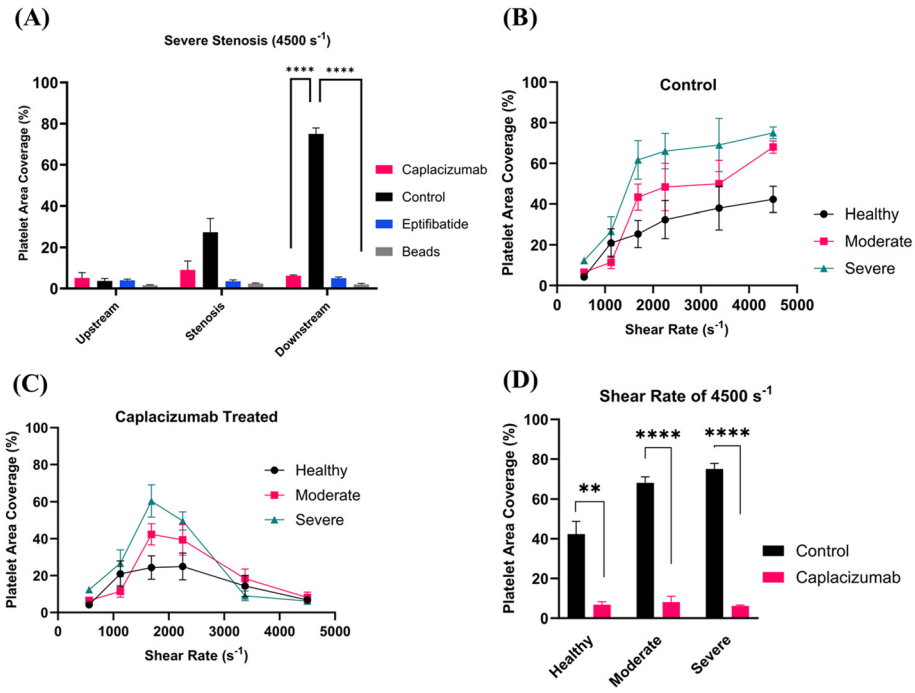

Fig. 10 Comprehensive analysis of platelet accumulation and caplacizumab's inhibitory effects across stenosis conditions. (A) Regional platelet coverage in severe stenosis (4500 s^{-1}) showing preferential downstream accumulation, effective inhibition by caplacizumab and eptifibatide, and minimal fluorescent bead deposition (****$p < 0.0001$ *vs.* control). (B) Shear rate-dependent platelet accumulation in control conditions demonstrating progressive increase with shear rate and stenosis severity. (C) Caplacizumab treatment showing maximum efficacy above 2250 s^{-1} across all stenosis conditions. (D) Caplacizumab effectiveness across stenosis severities at 4500 s^{-1} demonstrating consistent inhibition (**$p <$ 0.01, ****$p < 0.0001$ *vs.* respective control). Panels B–D quantify downstream region coverage (blue dashed box, Fig. 9B). Note: panels B and D show results at matched peak shear rates across geometries, with differences in platelet coverage reflecting varying local shear rate gradients. Data presented as mean ± SEM ($n = 3$).

designed to investigate platelet aggregation dynamics under precisely controlled shear conditions. Using the peak shear rate data from the computational analysis, specific flow rates for healthy, moderate and severe stenosis were selected to generate physiologically relevant peak shear rates (562, 1125, 1687, 2250, 3375, and 4500 s^{-1}) at the stenotic region. These targeted shear conditions allowed exploration of platelet behaviour across the range from moderate to high pathological shear rates identified in the CFD models. Fluorescence microscopy of $DiOC_6$-labeled platelets in severe stenosis revealed distinct shear rate-dependent aggregation patterns in control samples (Fig. 9, top row). The effective caplacizumab concentration (30 nM), determined from earlier aggregometry studies, was employed to evaluate inhibitory effects across these various shear conditions. At the lower peak shear rates (1125 s^{-1}), moderate and diffuse platelet accumulation was observed throughout the channel. When peak shear rates were increased to 3375 s^{-1} and 4500 s^{-1}, platelet aggregation became more pronounced and localized at the stenotic region, correlating with the areas of maximum shear stress identified in the CFD analysis (Fig. 6).

Time-course studies at 4500 s^{-1} demonstrated rapid thrombus formation in control conditions (Fig. 9, bottom panel). Substantial platelet accumulation was evident within the first 5 minutes, with continued growth observed through 10 minutes of perfusion. The spatial distribution of these aggregates corresponded to regions of high shear gradients identified in the computational analysis. Caplacizumab treatment significantly altered platelet accumulation patterns across all tested shear rates. The most pronounced inhibitory effect was observed at higher shear rates (3375 and 4500 s^{-1}), where control samples exhibited maximum aggregate formation. Time-series analysis at 4500 s^{-1} revealed that caplacizumab effectively prevented the formation of large platelet aggregates throughout the 10-minute observation period (Fig. 9, bottom panels), maintaining consistently low platelet adhesion even in regions of high shear stress.

To characterise the spatial distribution of platelet aggregation under physiologically relevant shear conditions, platelet area coverage was quantified in three distinct regions (defined in Fig. 9B) of the severe stenosis model including upstream, stenosis, and downstream regions (Fig. 10A). At 4500 s^{-1}, control samples demonstrated a distinctive pattern of platelet accumulation, with significantly enhanced coverage in the downstream region (75 ± 5%) compared to upstream (3.7 ± 2%, $p < 0.001$) and stenosis regions (27.3 ± 11.6%, $p < 0.003$). This pattern aligned with CFD-identified flow deceleration zones, consistent with enhanced post-stenotic platelet aggregation in previous studies.[10]

To confirm biological specificity, control experiments using 6 μm APC-conjugated fluorescent beads in PBS and platelet-poor plasma showed minimal accumulation (<2%

area coverage), confirming that observed aggregation represents platelet accumulation rather than flow-induced particle entrapment (Fig. 10A shows PBS control). Therapeutic validation with eptifibatide, a clinically established GPIIb/IIIa inhibitor, demonstrated comparable inhibitory efficacy to caplacizumab in the downstream region (5 ± 0.6% *vs.* 6.2 ± 0.4% coverage, respectively, $p = 0.15$). However, these agents differ fundamentally in their mechanistic scope and clinical implications.

Caplacizumab treatment significantly altered this spatial pattern of platelet accumulation. At 4500 s^{-1}, the drug markedly attenuated downstream platelet accumulation (6.2 ± 0.7% *vs.* 75 ± 5% control, $p < 0.0001$), while maintaining minimal effect on upstream (5.2 ± 4.4%) and stenosis regions (9 ± 7.5%). The pronounced inhibitory effect of caplacizumab specifically in the downstream (deceleration) region, suggested a mechanistic link between vWF-mediated platelet adhesion and local hemodynamic conditions. Based on these observations, subsequent analyses focused on this downstream region to further evaluate the relationship between stenosis severity and platelet accumulation.

Analysis of platelet accumulation under control conditions revealed a direct relationship between stenosis severity and shear rate-dependent platelet aggregation (Fig. 10B). In the severe stenosis model, platelet coverage increased sharply from 12.3 ± 1.4% at 562 s^{-1} to 66.1 ± 8.7% at 2250 s^{-1}, ultimately reaching 75.1 ± 2.9% at 4500 s^{-1}. The moderate stenosis condition showed a similar trend but with lower magnitudes, increasing from 6.6 ± 1% at 562 s^{-1} to 68.1 ± 3% at 4500 s^{-1}. The healthy model demonstrated the most gradual increase, reaching a maximum of 42.3 ± 6.5% at 4500 s^{-1}.

Quantification of platelet accumulation across varying shear rates demonstrated distinct response patterns in different stenosis geometries (Fig. 10C). At lower shear rates (562–1125 s^{-1}), minimal platelet accumulation was observed, with coverage values below 15% across all conditions. As shear rates increased, platelet coverage reached maximum values at 2250 s^{-1}, with the severe stenosis model showing the highest coverage (49.6 ± 4.9%), followed by moderate (39.3 ± 8.3%) and healthy conditions (24.9 ± 7.3%). Beyond 2250 s^{-1}, a significant decrease in platelet accumulation was observed across all stenosis conditions. This reduction was most pronounced in the severe stenosis model, where platelet coverage decreased from 49.6 ± 4.9% at 2250 s^{-1} to 6.2 ± 0.39% at 4500 s^{-1} ($p < 0.001$). Similar trends were observed in moderate stenosis (39.3 ± 8.3% to 8.1 ± 3%, $p < 0.05$) and healthy conditions (24.9 ± 7.3% to 6.8 ± 1.5%, $p > 0.05$). The sharp decline in platelet accumulation above 2250 s^{-1} was consistent across all geometries, with minimal differences between conditions at the highest tested shear rate (4500 s^{-1}).

The experimental design utilized matched peak shear rates across three stenosis geometries, allowing examination of how shear rate gradients influence platelet aggregation independently of peak shear magnitude. Under these controlled conditions (4500 s^{-1}), platelet coverage increased systematically with stenosis severity: healthy (42.3 ± 6.5%), moderate (68.1 ± 3%), and severe (75.1 ± 2.9%), a 77% increase from healthy to severe conditions (Fig. 10B and D), despite identical peak shear rates.

Analysis of the downstream region at high shear rate (4500 s^{-1}) demonstrated the inhibitory effect of caplacizumab across different stenosis severities (Fig. 10D). In healthy conditions, platelet area coverage was reduced from 42.3 ± 6.5% in control to 6.8 ± 1.5% with caplacizumab treatment ($p < 0.006$). Similar inhibitory effects were observed in moderate stenosis, where coverage decreased from 68.1 ± 3%

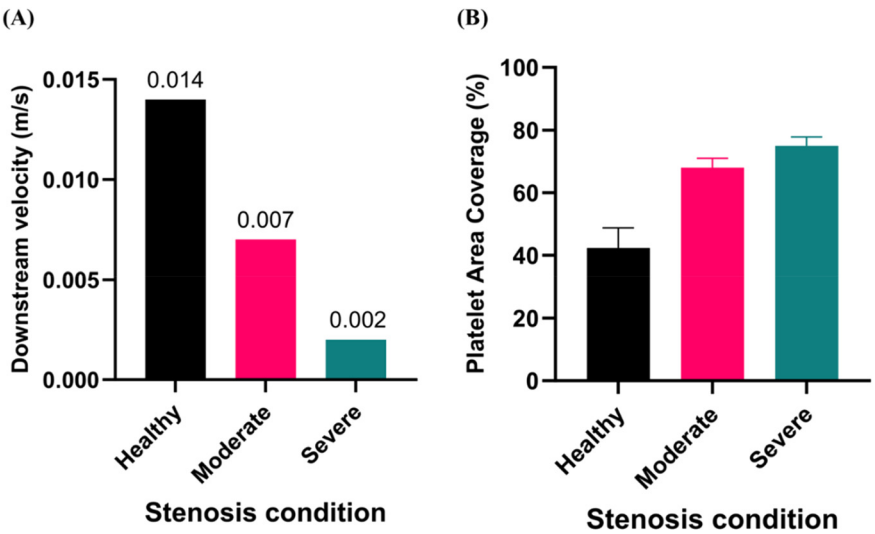

Fig. 11 Relationship between downstream flow velocity and platelet aggregation across stenosis severities at matched peak shear rate (4500 s^{-1}) in control conditions. (A) Area-averaged downstream velocity from CFD simulations decreases with increasing stenosis severity despite matched peak shear rates, reflecting lower flow rates, and thus lower velocities, required in severe stenosis to achieve equivalent peak shear rates. (B) Experimental platelet surface coverage in the downstream deceleration zone in control samples increases with stenosis severity under these conditions. Data in (B) presented as mean ± SEM ($n = 3$).

to 8.1 ± 3% ($p < 0.0001$), and in severe stenosis, where caplacizumab reduced coverage from 75.1 ± 2.9% to 6.2 ± 0.4% ($p < 0.0001$).

To examine the relationship between flow velocity and platelet aggregation, we quantified area-averaged downstream velocities in the downstream deceleration zone (blue quadrilateral region, Fig. 9B) across stenosis severities under matched peak shear conditions (4500 s^{-1}) and compared them to corresponding platelet surface coverage (Fig. 11). Downstream velocities decreased with increasing stenosis severity (healthy: 0.014 m s^{-1}; moderate: 0.007 m s^{-1}; severe: 0.002 m s^{-1}), while platelet surface coverage increased (healthy: 42.3 ± 6.5%; moderate: 68.1 ± 3.0%; severe: 75.1 ± 2.9%). This inverse relationship indicates that platelet aggregation increases as downstream velocity decreases, even under matched peak shear conditions.

Discussion

Thrombosis in aortic valve stenosis is primarily driven by shear-induced platelet aggregation, wherein pathological shear stress induce unfolding of von Willebrand factor (vWF), exposing the A1 domain for rapid binding to platelet GPIbα receptors.[40] This interaction occurs within ~10 milliseconds and does not require prior platelet activation, as demonstrated in recent studies.[7] The experimental results show that shear rates characteristic of stenotic regions (2250–4500 s^{-1}) are sufficient to initiate vWF unfolding and GPIbα binding. The downstream deceleration zone provides favourable conditions for platelet aggregate stabilization and growth due to reduced dispersive forces and increased residence time. These observations, including the inhibitory effect of caplacizumab, confirm the critical role of vWF–GPIbα interactions in this thrombotic pathway and align with current mechanistic understanding of SIPA. Prior studies have shown that vWF unfolding begins at shear rates around 2000–5000 s^{-1},[41,42] and the present results are consistent with these thresholds, with notable aggregation observed from approximately 2250 s^{-1} onward (Fig. 10D).

Flow cytometry experiments in the present study provided detailed mechanistic insights, demonstrating reduction in the median fluorescence intensity of vWF-bound platelets in the presence of caplacizumab. The observation of partially restored GPIb receptor availability, evidenced by increased CD42b MFI during caplacizumab treatment in our experiments, reveals the drug's specific mechanism in preventing vWF–GPIb interactions while preserving receptor functionality. This specificity was further supported by the platelet aggregation assays performed in this study, showing selective inhibition of ristocetin-induced but not ADP-induced aggregation. These findings are consistent with previous research[38] and suggest minimal interference with normal hemostatic functions.

The CFD analysis revealed critical hemodynamic features that underlie thrombogenic potential in stenotic valve conditions. The transition from uniform flow in healthy conditions to highly heterogeneous patterns in severe stenosis was characterized by dramatic increases in local shear rates. Particularly significant was the computational identification of distinct acceleration and deceleration zones, where sharp spatial gradients in shear rate (approximately 2×10^8 s^{-1} μm^{-1}) would create conditions favourable for platelet activation and aggregation (Fig. 6). The correlation between these high-gradient regions and subsequent platelet accumulation is demonstrated in the experimental results (Fig. 9).

The spatial distribution of wall shear stress, particularly the sharp transitions observed at stenosis entry and exit points, identifies potential sites for platelet activation and adhesion. These computational findings provide a mechanistic framework for understanding the enhanced platelet accumulation observed in our experimental studies. The identification of distinct high-shear activation zones and low-velocity deceleration regions demonstrate that high shear stress activates platelets *via* vWF unfolding, steep shear gradients amplify this activation, and downstream regions with reduced flow velocity allow activated platelets to aggregate into stable thrombi.

The microfluidic model included recessed regions designed to replicate the anatomical sinuses of the aortic valve. While platelet-associated fluorescence was observed in these areas, even with caplacizumab treatment, these regions were excluded from quantitative analysis due to their distinct hemodynamic characteristics. These recessed geometries are known to experience markedly low wall shear stress and recirculatory flow patterns,[43] promoting passive platelet trapping rather than shear-induced vWF–GPIbα adhesion. Under such low-shear conditions, platelet aggregation likely occurs *via* alternative pathways (*e.g.*, fibrinogen–αIIbβ3),[4] explaining persistent platelet signals despite vWF inhibition. These findings highlight that multiple thrombotic mechanisms may operate in spatially distinct hemodynamic zones of the stenotic valve, suggesting that complementary therapies may be required to manage thrombosis risk beyond high-shear regions.

The experimental approach required varying inlet flow rates to achieve equivalent peak shear rates across different stenosis geometries, creating distinct velocity profiles and platelet residence times across geometries.[44,45] This design reflects the physiological reality where cardiac output remains relatively constant while valve cross-sectional area decreases with disease progression. While peak shear rates were systematically matched across stenosis geometries in experimental comparisons, CFD analysis revealed that corresponding shear rate gradients varied by over an order of magnitude (Fig. 8A). This design enabled isolation of gradient-specific effects. The 77% increase in platelet coverage from healthy to severe stenosis, despite identical peak shear, highlights the mechanistic importance of shear gradients. The spatial correspondence between high-gradient downstream regions and sites of maximal platelet accumulation (Fig. 10A) provides direct evidence that local shear rate gradients, rather than peak shear stress alone, drive platelet aggregation in stenotic flow environments. This

gradient-driven mechanism is consistent with prior studies demonstrating that abrupt shear transitions and steep spatial gradients can promote von Willebrand factor unfolding and platelet activation under pathological flow conditions.[46,47]

Importantly, multiple lines of evidence demonstrate that shear gradient-dependent mechanisms, rather than residence time effects, drive the observed platelet behavior: the preferential platelet accumulation in downstream deceleration zones correlating with CFD-predicted gradient regions (Fig. 10A), the consistent 2250 s^{-1} activation threshold across all geometries despite varying residence times (Fig. 10C and D), and caplacizumab's specific efficacy against shear-activated vWF pathways. These findings consistently indicate that platelet accumulation patterns correlate strongly with regions of steep shear gradients, suggesting that mechanical forces rather than residence time alone drive the enhanced thrombosis risk observed in severe stenosis.

This interpretation is further supported by the inverse relationship between local flow velocity and platelet aggregation across stenosis severities (Fig. 11), where lower velocities in severe stenosis correspond to higher aggregation despite matched peak shear rates. This confirms that flow velocity and residence time do not independently account for the observed thrombotic patterns. These results align with prior studies demonstrating that spatial shear gradients, particularly in deceleration zones, are critical determinants of platelet aggregation and represent the dominant mechanical driver of thrombus formation under high-shear conditions.[24,46,47]

The presented microfluidic experiments provided compelling evidence for caplacizumab's selective inhibition of shear-induced platelet aggregation, particularly above 2250 s^{-1}. Visual inspection of platelet deposition patterns reveals preferential accumulation in the stenotic throat region where computational analysis shows maximum shear gradients (Fig. 6 and 9A). This phenomenon, attributed to higher shear gradients in severe stenosis, extends previous work by Nesbitt *et al.*[24] on shear gradient-dependent platelet behaviour to the specific context of aortic valve stenosis.

The comprehensive validation studies using fluorescent beads and eptifibatide comparisons provide critical context for our findings. The negligible accumulation of inert particles confirms that the stenosis model captures genuine biological platelet aggregation rather than flow artifacts. While eptifibatide demonstrates comparable acute efficacy, its broad GPIIb/IIIa inhibition across all shear conditions is associated with increased bleeding complications in clinical practice.[48] Caplacizumab's selective inhibition of vWF–GPIbα interactions specifically under pathological shear conditions (>2250 s^{-1}) represents a mechanistically targeted approach that may preserve normal hemostatic function while preventing pathological thrombosis, a critical advantage in treating high-shear cardiovascular conditions.

For clinical translation, this shear-dependent mechanism enables targeted therapy. Doppler echocardiography provides peak aortic jet velocities that correlate with stenotic shear rates, while 4D flow MRI can directly quantify wall shear stress.[49] Patient-specific computational modeling based on imaging data can also predict individual shear environments.[50] These non-invasive approaches could guide therapeutic decision-making by identifying patients whose stenotic conditions generate the high shear rates where caplacizumab demonstrates optimal efficacy. The designed aortic valve microfluidic model has potential applications in cardiovascular medicine by providing a platform that could eventually enable patient-specific thrombosis modelling. Its ability to replicate individual stenosis geometries while testing patient blood samples under physiological conditions bridges the gap between *in vitro* molecular studies and *in vivo* outcomes.

Study limitations and future directions

The microfluidic model successfully demonstrates caplacizumab's efficacy in mitigating shear-induced thrombosis and provides novel mechanistic insights into aortic valve stenosis; however, several experimental considerations merit discussion for future clinical translation. Utilized microfluidic approach achieves precise control of physiologically relevant shear rate conditions that effectively capture the critical thresholds for vWF-mediated platelet activation. Nevertheless, the scaled geometry and steady-flow conditions, though enabling systematic investigation of shear-dependent mechanisms, differ from the complex pulsatile dynamics and three-dimensional valve architecture *in vivo*. The rectangular channel design and absence of mobile valve components represent necessary simplifications that facilitated the core mechanistic discoveries yet create opportunities for enhanced geometric fidelity in future iterations.

The absence of endothelial lining, although enabling isolation of direct shear-platelet–vWF interactions, represents an area for model enhancement. Endothelial cells significantly modulate hemostasis through vasoactive mediator release and local vWF production, particularly under the dysfunctional conditions present in aortic stenosis. Future endothelialized vasculature-on-chip platforms could build upon these foundational findings to incorporate these additional biological complexities. The computational simulations operated within the laminar regime ($Re < 100$), which effectively captured the primary shear-activation mechanisms despite differing from potential turbulent flow conditions in severe stenoses.

The continuum-based CFD model does not account for discrete cellular phenomena that become dominant in microchannels below ~100 μm, including cell-free layer formation, platelet margination, and spatially heterogeneous hematocrit distribution. The model likely overestimates near-wall shear stress due to the absence of plasma-rich cell-free layers. Importantly, these limitations do not compromise the primary conclusions because: (1) key findings derive from direct experimental observations in microfluidic systems using whole blood, where all relevant microscale phenomena are naturally present; and (2) the CFD simulations served solely as tools for experimental parameter selection and relative geometric

comparisons. Building upon these findings, future studies employing cell-resolved modeling approaches could offer complementary insights into microscale platelet transport mechanisms in stenotic flow environments.

Additionally, the use of healthy donor blood, essential for establishing reproducible baseline drug responses, provides a foundation for future studies incorporating patient-derived samples with their inherent vWF multimer variations and altered platelet reactivity. These strategic limitations highlight clear pathways for advancing this promising therapeutic approach through pulsatile flow validation, patient-specific modeling, and combination therapy optimization.

Conclusion

This study demonstrates caplacizumab's potential in preventing thrombosis in aortic valve stenosis through a novel microfluidic model and comprehensive experimental approach. These findings reveal caplacizumab's efficacy in inhibiting platelet aggregation under high shear stress conditions characteristic of severe stenosis. The unique contribution of this variable shear gradient analysis provides new insights into platelet aggregation mechanisms, showing increased aggregation with stenosis severity despite constant peak shear rates, as the geometrical differences create varying spatial distributions of shear stress. This work represents the first evaluation of caplacizumab as a potential therapeutic intervention for aortic valve stenosis, offering a possible adjunctive therapy that could potentially reduce thrombotic complications associated with the disease. The integration of microfluidic experimentation with computational fluid dynamics establishes a platform for creating personalized thrombosis models that can optimize antithrombotic strategies before *in vivo* administration. While these results are promising, further clinical trials are necessary to validate caplacizumab's long-term efficacy and safety in this specific clinical context.

Author contributions

CEH provided the rationale for the study. SG and CEH obtained funding. SZS, DR, and MN designed the aortic valve configuration. MK and MA conducted CFD simulations. SZS conducted flow cytometry experiments. SZS, DR, and SP conducted the microfluidic and platelet aggregation experiments. JC contributed to the design and interpretation of the microfluidic experiments. SZS conducted the CFD and experimental data interpretation and statistical analysis. SZS wrote the first draft of the manuscript. JC, KA, SG, and CEH provided critical feedback and supervision throughout the project. All authors reviewed the manuscript.

Conflicts of interest

The authors declare that they have no competing interests.

Data availability

All data supporting the findings presented in this study are included within the manuscript.

Acknowledgements

This work was supported by Monash University. S. D. G would like to acknowledge the support of the National Health and Medical Research Council (NHMRC) (grant numbers: 2016995 and APP2002567) and National Heart Foundation (Fellowship number 106675). C. E. H is a Senior Research Fellow of the NHMRC (award number GNT1154270). We acknowledge Sanofi for providing Caplacizumab for this study (no financial support was received). While Sanofi reviewed the manuscript before submission, they were not involved in the study's development, conduct, analysis, or reporting of results. The authors thank ARAFlowCore for their assistance with flow cytometry. This work was performed in part at the Melbourne Centre for Nanofabrication (MCN) in the Victorian Node of the Australian National Fabrication Facility (ANFF). The authors thank Monash Micro Imaging (MMI) for providing access to microscopy facilities and technical support. We would like to thank the volunteers who donated their blood for this experiment.

References

1 P. Unger, X. Galloo and P. Pibarot, *Eur. Heart J.*, 2025, ehaf116.
2 M. J. Czarny and J. R. Resar, *Clin. Med. Insights: Cardiol.*, 2014, **8**(1), 15–24.
3 P. Bańka, M. Wybraniec, T. Bochenek, B. Gruchlik, A. Burchacka, A. Swinarew and K. Mizia-Stec, *J. Clin. Med.*, 2023, **12**, 6301.
4 A. Rana, E. Westein, B. Niego and C. E. Hagemeyer, *Front. Cardiovasc. Med.*, 2019, **6**, 141.
5 P. Bańka, M. Wybraniec, T. Bochenek, B. Gruchlik, A. Burchacka, A. Swinarew and K. Mizia-Stec, *J. Clin. Med.*, 2023, **12**(19), 6301.
6 Z. M. Ruggeri, *Thromb. Res.*, 2007, **120**, S5–S9.
7 Z. L. Liu, C. Bresette, C. K. Aidun and D. N. Ku, *Blood Adv.*, 2022, **6**, 2453–2465.
8 L. D. Casa, D. H. Deaton and D. N. Ku, *J. Vasc. Surg.*, 2015, **61**, 1068–1080.
9 E. Mammadova-Bach, T. Gudermann and A. Braun, *Arterioscler., Thromb., Vasc. Biol.*, 2023, **43**, 1339–1348.
10 W. S. Nesbitt, E. Westein, F. J. Tovar-Lopez, E. Tolouei, A. Mitchell, J. Fu, J. Carberry, A. Fouras and S. P. Jackson, *Nat. Med.*, 2009, **15**, 665–673.
11 D. Bluestein, W. Yin, K. Affeld and J. Jesty, *J. Heart Valve Dis.*, 2004, **13**, 501–508.
12 C. M. Otto and B. Prendergast, *N. Engl. J. Med.*, 2014, **371**, 744–756.
13 S. Zeibi Shirejini, J. Carberry, K. Alt, S. D. Gregory and C. E. Hagemeyer, *Adv. Funct. Mater.*, 2023, **33**, 2303717.
14 H. S. Markus, C. McCollum, C. Imray, M. A. Goulder, J. Gilbert and A. King, *Stroke*, 2011, **42**, 2149–2153.

15 P. Jilma-Stohlawetz, J. C. Gilbert, M. E. Gorczyca, P. Knöbl and B. Jilma, *Thromb. Haemostasis*, 2011, **106**, 391–397.
16 R. R. Schimmer, T. Sutter, A. Bachofner, E. Ranieri, A. K. Rodewald, J. A. Kremer Hovinga, N. Kimmich, A. Trinchero and J. D. Studt, *Br. J. Haematol.*, 2024, **204**, 1994–1998.
17 M. Scully, S. R. Cataland, F. Peyvandi, P. Coppo, P. Knöbl, J. A. Kremer Hovinga, A. Metjian, J. de la Rubia, K. Pavenski and F. Callewaert, *N. Engl. J. Med.*, 2019, **380**, 335–346.
18 J. Sedlak and A. Clyne, in *Mechanobiology: Methods and Protocols*, Springer, 2023, pp. 81–90.
19 C. Ye, S. Ali, Q. Sun, M. Guo, Y. Liu, Y. Gao and B. Huo, *Comput. Biol. Med.*, 2019, **106**, 140–148.
20 M. N. de Graaf, A. Vivas, D. G. Kasi, F. E. van den Hil, A. van den Berg, A. D. van der Meer, C. L. Mummery and V. V. Orlova, *Lab Chip*, 2023, **23**, 168–181.
21 Y. Qiu, C. Lu, F. Bao and G. Hu, *Lab Chip*, 2023, **23**, 4302–4312.
22 C.-S. Jhun, R. Newswanger, J. P. Cysyk, S. Ponnaluri, B. Good, K. B. Manning and G. Rosenberg, *ASAIO J.*, 2021, **67**, 666–674.
23 Y. C. Zhao, P. Vatankhah, T. Goh, R. Michelis, K. Kyanian, Y. Zhang, Z. Li and L. A. Ju, *Sci. Rep.*, 2021, **11**, 6875.
24 W. S. Nesbitt, E. Westein, F. J. Tovar-Lopez, E. Tolouei, A. Mitchell, J. Fu, J. Carberry, A. Fouras and S. P. Jackson, *Nat. Med.*, 2009, **15**, 665–673.
25 Y. Qiu, J. Lin, A. Wang, Z. Fang, Y. Sakurai, H. Choi, E. K. Williams, E. T. Hardy, K. Maher and A. F. Coskun, *Nature*, 2025, 1–11.
26 J. Berry, F. J. Peaudecerf, N. A. Masters, K. B. Neeves, R. E. Goldstein and M. T. Harper, *Lab Chip*, 2021, **21**, 4104–4117.
27 W. M. Swanson and R. E. Clark, *Circ. Res.*, 1974, **35**, 871–882.
28 C. T. Riche, C. Zhang, M. Gupta and N. Malmstadt, *Lab Chip*, 2014, **14**, 1834–1841.
29 L. D. Casa and D. N. Ku, *Cardiovasc. Eng. Technol.*, 2014, **5**, 154–163.
30 C. Szydzik, R. J. Brazilek, K. Khoshmanesh, F. Akbaridoust, M. Knoerzer, P. Thurgood, I. Muir, I. Marusic, H. Nandurkar and A. Mitchell, *Lab Chip*, 2018, **18**, 1778–1792.
31 A. P. Yoganathan, K. Chandran and F. Sotiropoulos, *Ann. Biomed. Eng.*, 2005, **33**, 1689–1694.
32 S. T. Gould, S. Srigunapalan, C. A. Simmons and K. S. Anseth, *Circ. Res.*, 2013, **113**, 186–197.
33 P. Youssefi, A. Gomez, T. He, L. Anderson, N. Bunce, R. Sharma, C. A. Figueroa and M. Jahangiri, *J. Thorac. Cardiovasc. Surg.*, 2017, **153**, 8–20, e23.
34 R. Tuna, W. Yi, E. Crespo Cruz, J. Romero, Y. Ren, J. Guan, Y. Li, Y. Deng, D. Bluestein and Z. L. Liu, *Int. J. Mol. Sci.*, 2024, **25**, 4800.
35 H. Lei, D. A. Fedosov, B. Caswell and G. E. Karniadakis, *J. Fluid Mech.*, 2013, **722**, 214–239.
36 Y. Shen, G. M. Romo, J.-f. Dong, A. Schade, L. V. McIntire, D. Kenny, J. C. Whisstock, M. C. Berndt, J. A. López and R. K. Andrews, *Blood*, 2000, **95**, 903–910.
37 J.-F. Dong, M. C. Berndt, A. Schade, L. V. McIntire, R. K. Andrews and J. A. López, *Blood*, 2001, **97**, 162–168.
38 M. Scully, S. R. Cataland, F. Peyvandi, P. Coppo, P. Knöbl, J. A. Kremer Hovinga, A. Metjian, J. de la Rubia, K. Pavenski, F. Callewaert, D. Biswas, H. De Winter and R. K. Zeldin, *N. Engl. J. Med.*, 2019, **380**, 335–346.
39 S. P. Jackson, *Blood*, 2007, **109**, 5087–5095.
40 T. A. Springer, *Blood*, 2014, **124**, 1412–1425.
41 S. M. Rahman and V. Hlady, *Lab Chip*, 2021, **21**, 174–183.
42 E. F. Yeo, J. M. Oliver, N. Korin and S. L. Waters, *Biomech. Model. Mechanobiol.*, 2024, **23**, 1299–1317.
43 D. Oks, S. Reza, M. Vázquez, G. Houzeaux, B. Kovarovic, C. Samaniego and D. Bluestein, *medRxiv*, 2023, preprint, DOI: **10.1101/2023.11.13.23298476**.
44 C. Menichini and X. Y. Xu, *J. Math. Biol.*, 2016, **73**, 1205–1226.
45 V. Rayz, L. Boussel, L. Ge, J. Leach, A. Martin, M. Lawton, C. McCulloch and D. Saloner, *Ann. Biomed. Eng.*, 2010, **38**, 3058–3069.
46 N. A. Zainal Abidin, E. K. W. Poon, C. Szydzik, M. Timofeeva, F. Akbaridoust, R. J. Brazilek, F. J. Tovar Lopez, X. Ma, C. Lav, I. Marusic, P. E. Thompson, A. Mitchell, A. S. H. Ooi, J. R. Hamilton and W. S. Nesbitt, *BMC Biol.*, 2022, **20**, 73.
47 F. J. Tovar-Lopez, G. Rosengarten, E. Westein, K. Khoshmanesh, S. P. Jackson, A. Mitchell and W. S. Nesbitt, *Lab Chip*, 2010, **10**, 291–302.
48 G. Tonin and J. Klen, *Int. J. Mol. Sci.*, 2023, **24**, 5446.
49 Y. Shan, J. Li, Y. Wang, B. Wu, A. J. Barker, M. Markl, C. Wang, X. Wang and X. Shu, *J. Thorac. Cardiovasc. Surg.*, 2017, **153**, 1263–1272, e1261.
50 E. L. Manchester, S. Pirola, M. Y. Salmasi, D. P. O'Regan, T. Athanasiou and X. Y. Xu, *Front. Bioeng. Biotechnol.*, 2022, **10**, 836611.